Real-Time Network-Aware Roadside LiDAR Data Compression

Md Parvez Mollah[1][a], Murugan Sankaradas[2][b], Ravi K. Rajendran[2][c] and Srimat T. Chakradhar[2][d]

[1]*Department of Computer Science, The University of New Mexico, Albuquerque, New Mexico, U.S.A.*

[2]*NEC Laboratories America, Inc., Princeton, New Jersey, U.S.A.*

parvez.supto@gmail.com, {murugs, rarajendran, chak}@nec-labs.com

Keywords: Roadside LiDAR, Background Subtraction, Sensor-Agnostic Compression, Cloud, Edge Systems.

Abstract: LiDAR technology has emerged as a pivotal tool in Intelligent Transportation Systems (ITS), providing unique capabilities that have significantly transformed roadside traffic applications. However, this transformation comes with a distinct challenge: the immense volume of data generated by LiDAR sensors. These sensors produce vast amounts of data every second, which can overwhelm both private and public 5G networks that are used to connect intersections. This data volume makes it challenging to stream raw sensor data across multiple intersections effectively. This paper proposes an efficient real-time compression method for roadside LiDAR data. Our approach exploits a special characteristic of roadside LiDAR data: the background points are consistent across all frames. We detect these background points and send them to edge servers only once. For each subsequent frame, we filter out the background points and compress only the remaining data. This process achieves significant temporal compression by eliminating redundant background data and substantial spatial compression by focusing only on the filtered points. Our method is sensor-agnostic, exceptionally fast, memory-efficient, and adaptable to varying network conditions. It offers a 2.5x increase in compression rates and improves application-level accuracy by 40% compared to current state-of-the-art methods.

1 INTRODUCTION

The advent of Intelligent Transportation Systems (ITS) has ushered in a new era of innovation and efficiency in managing our road networks. At the heart of this transformation lies the need for real-time, accurate, and comprehensive data that empowers traffic authorities to make informed decisions, enhances road safety, and eases the daily commute for millions of travelers. In this context, Light Detection and Ranging (LiDAR) technology has emerged as a pivotal tool, offering unique capabilities that have reshaped the landscape of roadside traffic applications.

Unlike conventional camera-based systems, LiDAR sensors provide a dynamic and precise understanding of traffic dynamics and road conditions. Their ability to capture high-resolution, three-dimensional data equips them to excel in applications such as traffic monitoring, congestion management, pedestrian safety, and infrastructure assessment. The advantages of LiDAR over cameras are evident. For instance, as illustrated in Figure 1, 3D reconstruction errors for cameras increase as the distance grows (Li and Yoon, 2023). Additionally, cameras exhibit reduced performance in low light, particularly at night, where their effectiveness diminishes by approximately 20% for every meter (refer to Figure 2). In contrast, LiDAR operates independently of ambient light, ensuring reliability both day and night, and possesses depth perception capabilities that facilitate precise object detection and tracking even in complex, cluttered environments. Consequently, LiDAR proves better suited for roadside traffic applications.

Private 5G networks are proposed in traffic intersection applications by operators to interconnect intersections, because they offer high bandwidth, low latency, security, and control. The context to deploy LiDARs at traffic intersections and connect them with private 5G networks to transmit the data to the cloud, enabling real-time analytics for roadside traffic applications (as shown in Figure 3). LiDAR is a promising technology for traffic applications, but its high data volume is a challenge. Private 5G cannot stream raw data from sensors across multiple intersections. This challenge underscores the pressing need for the development of efficient data compression methods tai-

[a] https://orcid.org/0000-0002-7131-1354
[b] https://orcid.org/0000-0002-4608-1630
[c] https://orcid.org/0009-0002-3663-8869
[d] https://orcid.org/0000-0003-3530-3901

Mollah, M. P., Sankaradas, M., Rajendran, R. K. and Chakradhar, S. T.
Real-Time Network-Aware Roadside LiDAR Data Compression.
DOI: 10.5220/0013298900003941

In *Proceedings of the 11th International Conference on Vehicle Technology and Intelligent Transport Systems (VEHITS 2025)*, pages 136-147
ISBN: 978-989-758-745-0; ISSN: 2184-495X

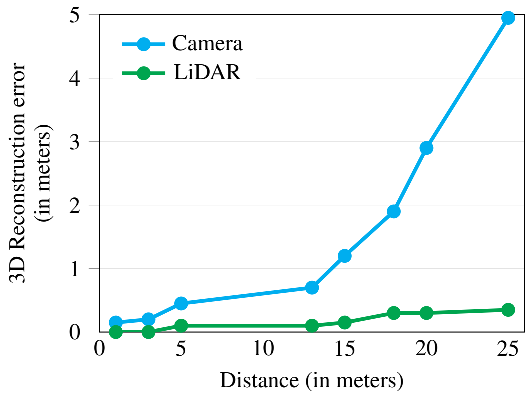

Figure 1: 3-D reconstruction error comparison for cameras and LiDARs (Li and Yoon, 2023).

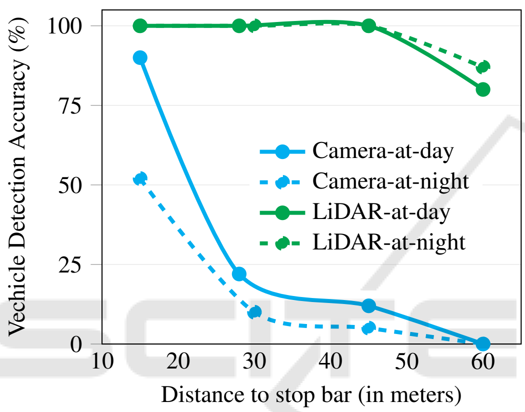

Figure 2: Camera vs LiDAR performance comparison in different lighting condition (Guan et al., 2023).

lored specifically to roadside LiDAR data.

To develop such a technique, we need to address three challenges. First, the compression method must be capable of running on low-cost computing devices to reduce installation costs. Second, the compression must be sensor-agnostic, meaning it should work with different types of LiDAR scanning patterns. It should also be network-aware to handle fluctuating network speeds, as the network will be shared among many devices. Third, LiDAR data must be made available in real-time at the edge or in the cloud for processing and further analytics.

In this paper, we develop an efficient real-time compression method by exploiting a unique characteristic of roadside LiDAR data: the background points in roadside LiDARs are repeated across all frames. Our idea is to detect and send the background points to the cloud only once. Subsequently, we filter the background points for each frame and only compress the filtered frames. By filtering the backgrounds, our method achieves substantial temporal compression, and by compressing only the filtered points, it gains significant spatial compression as well.

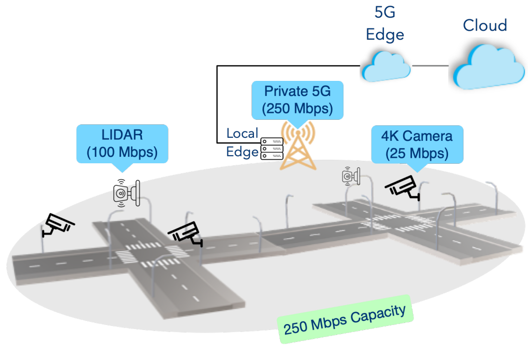

Figure 3: Deployment of LiDAR sensors at the traffic intersections and connecting them with shared private 5G network.

Our key contributions of this paper are as follows:

- We propose a novel compression scheme for roadside LiDAR data that filters out background points from frames before compression, as these points are unnecessary for downstream applications.
- We propose an extremely fast and memory efficient background detection and filtering technique that can be used with other existing point cloud compression methods to increase their efficiency.
- We develop a sensor-agnostic, real-time network-aware point cloud compression mechanism for roadside LiDARs. To the best of our knowledge, this is the first work that can adapt compression rate based on the available network bandwidth.
- Our compression system achieves 2.5x higher compression rates with faster compression speeds and minimal reconstruction errors compared to state-of-the-art compression methods. Moreover, our method achieves higher application-level accuracy compared to the best alternative.

2 RELATED WORK

2.1 Background Detection and Filtering

The task of background detection and filtering from the roadside LiDAR data has been widely explored in recent years. Most of the works in literature can be categorized into two groups based on the methodology used: i) density-based (Wu et al., 2018; Lv et al., 2019; Lin et al., 2023) ii) feature-based (Zhao et al., 2019; Zhao et al., 2023).

Density-based methods divide the entire 3-D space into smaller cubes and compute the point density of each cube for a certain amount of time. The idea is that the density of background points will be higher than moving object points for static LiDARs. To find a density threshold to separate the background points, (Wu et al., 2018) uses the density value where the slope of the frequency curve of the point densities becomes positive. In (Lin et al., 2023), the authors perform several steps such as identifying road user passing area, removing outliers using DBSCAN algorithm, etc., on top of computing density of cubes. The main limitation of density-based methods is that working in 3D space require huge amount of memory, which is not feasible to deploy in low-cost computation units on traffic poles.

Feature-based methods exploit the characteristics of the point cloud data to identify the background points. For example, (Zhao et al., 2019) detects and filters the background points by comparing the heights between raw LiDAR data and background objects based on laser channels and azimuth angles. In (Zhao et al., 2023), a 2D channel-azimuth background table is generated by learning the critical distance information of both static and dynamic backgrounds. Feature-based methods do not suffer from memory inefficiency, however, they require $100-300$ milliseconds to filter backgrounds from a frame, which is expensive for our case.

Existing works treat background detection and filtering as a single task. For them, a few gigabytes of memory or a few hundred milliseconds of time suffice. However, in our case, background detection must be memory-efficient, as it will operate on low-cost devices. Furthermore, background filtering must be exceptionally fast, as we need to run the compression mechanism on top of it.

2.2 Compression

Various compression methods have been proposed in literature for point cloud data. The most used method for encoding point cloud data typically involves the utilization of space-partitioning trees, with Octree being the predominant choice (Golla and Klein, 2015; Lasserre et al., 2019; Thanou et al., 2016). The G-PCC technique, a part of the MPEG point cloud compression standard, also falls within this category (Lasserre et al., 2019). Each leaf node of the Octree can be encoded using either a single occupancy bit, which can be lossless when each leaf node contains precisely one point, or through plane extraction, which preserves more intricate details when multiple points reside within a leaf node. G-PCC offers both of these encoding options. Building upon the foundation of space-partitioning tree representation, prior research has explored diverse strategies to mitigate redundant information, such as employing motion compensation in 3D space (Thanou et al., 2016), or directly applying video compression techniques (Golla and Klein, 2015). Google also develops a generalized method for compressing 3-D meshes and point clouds (Google, 2018). While these approaches prove effective in specific use cases, one drawback of unstructured representations is their failure to exploit the distinctive characteristics exposed by LiDAR point clouds, resulting in generally lower compression rates.

Another family of works convert point clouds into 2-D images using spherical projection (Sun et al., 2019; Tu et al., 2019) or orthogonal projection (Krivokuća et al., 2020) and then use existing image/video compression methods to compress the projected images. Due to applying image and video compression algorithms, these methods fail to retain the inherent spatial information within the point cloud, which typically leads to reduced accuracy in down-the-pipeline applications.

Some recent works focus on specific use cases of LiDARs and develop compression techniques only suitable for those use cases (Feng et al., 2020; Mollah et al., 2022). For example, (Feng et al., 2020) compresses point cloud data from moving LiDARs by using coordinate transformation and 3-D plane fitting, whereas (Mollah et al., 2022) proposes a batch compression technique for roadside LiDARs by using wavelet decomposition to capture quick transition of vehicles.

Since our goal is to enable massive device connectivity and stream data in real-time, we need a compression mechanism with strict bandwidth and latency requirements. None of the existing methods are suitable for our case as they fail to meet either the bandwidth or the latency requirements while keeping down-the-pipeline application accuracy.

3 PROPOSED SYSTEM

3.1 System Architecture

In this section, we provide a brief overview of our proposed system. Figure 4 illustrates a block diagram of how the components of our system interact with each other. Our system comprises two primary components: i) the Background Extraction Module, and ii) the Compression Module.

The task of the Background Extraction Module is to identify background points by analyzing a set of raw LiDAR frames. To accomplish this, it computes

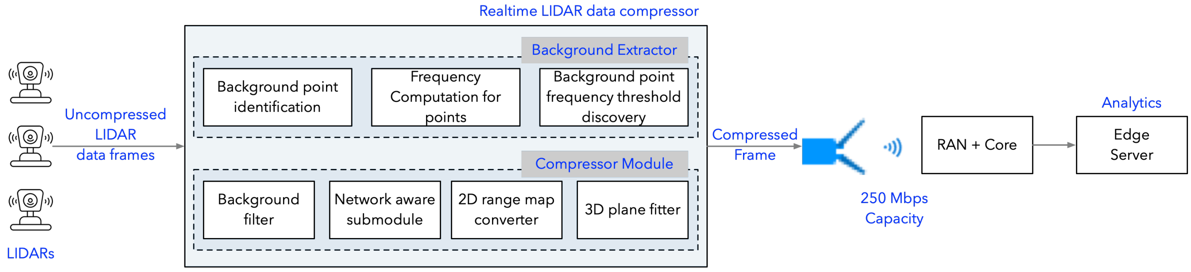

Figure 4: Block diagram of our proposed compression system.

the frequency of each point across the set of frames and determines a frequency threshold to separate the background points. Once the background points are identified, they are stored within the system for use by the Compression Module.

The Compression Module, on the other hand, takes a raw LiDAR frame, filters out the background, and then determines the size of the range map using the network-aware sub-module. Subsequently, the filtered frame is converted into a range map, and a 3-D plane fitting method is applied to compress the frame. The compressed frame is then transmitted to the edge via the 5G network for real-time analytics.

3.2 Background Detection and Filtering

The key idea of our background detection and filtering techniques involves transforming the 3-D point cloud frame into a 2-D grid, referred to as a range map, through spherical projection. This conversion serves the purpose of grouping the 3-D points into discrete buckets, enabling the counting of their frequencies across all frames.

To convert each point (x,y,z) of a point cloud frame to a value r at index (ϕ,θ) in the range map:

$$r = \sqrt{x^2+y^2+z^2}, \tag{1}$$

$$\phi = \lfloor \arccos(\frac{z}{r})/\phi_l \rfloor, \theta = \lfloor \arctan(\frac{x}{y})/\theta_l \rfloor, \tag{2}$$

where ϕ_l and θ_l are the vertical and horizontal resolutions of the LiDAR, respectively.

Algorithm 1 describes how our background detection works. The algorithm takes a stream of point cloud frames $\mathcal{P}$ (usually 5 minutes of frames), vertical and horizontal resolutions of LiDAR ϕ_l and θ_l, LiDAR's vertical and horizontal field of view V and H, and a nearest neighbor distance threshold D_t as inputs and outputs a set of 3-D points which are identified as background points. The algorithm works as follows:

At first, the dimensions of the range map are computed (line 1), and an empty 2-D range map *r_map* with the computed dimensions is initialized (line 2).

Algorithm 1: Background Detection Algorithm.

Require: A set of point cloud frames $\mathcal{P}$ with n frames, LiDAR vertical resolution ϕ_l, LiDAR horizontal resolution θ_l, LiDAR V-FoV V, LiDAR H-FoV H, nearest neighbor distance threshold D_t

Ensure: A set of (x,y,z) points, which are detected as background points

1: $rows \leftarrow \frac{V}{\phi_l}, cols \leftarrow \frac{H}{\theta_l}$
2: $r\_map(1:rows, 1:cols) \leftarrow \emptyset$
3: **for** each frame $p \in \mathcal{P}$ **do**
4:   **for** each point $(x,y,z) \in p$ **do**
5:     $d \leftarrow \sqrt{x^2+y^2+z^2}$
6:     $r \leftarrow \lfloor \arccos(\frac{z}{d})/\phi_l \rfloor$
7:     $c \leftarrow \lfloor \arctan(\frac{x}{y})/\theta_l \rfloor$
8:     $(x_n,y_n,z_n) \leftarrow NN(r\_map(r,c),(x,y,z),D_t)$
9:     **if** $(x_n,y_n,z_n) \neq \emptyset$ **then**
10:       $updateFrq(r\_map(r,c),(x_n,y_n,z_n))$
11:     **else**
12:       $insert(r\_map(r,c),(x,y,z,1))$
13:     **end if**
14:   **end for**
15: **end for**
16: $fr \leftarrow \emptyset$
17: **for** for each $(x,y,z,c) \in r\_map$ **do**
18:   $fr(c) \leftarrow fr(c)+1$
19: **end for**
20: $fr\_threshold \leftarrow 0$
21: $keys \leftarrow getMapKeys(fr)$
22: **for** $i \leftarrow 2 : length(keys)$ **do**
23:   **if** $fr(keys(i)) - fr(keys(i-1))$ **then**
24:     $fr\_thresold \leftarrow keys(i)$
25:     break
26:   **end if**
27: **end for**
28: $bg\_points \leftarrow \emptyset$
29: **for** for each $(x,y,z,c) \in r\_map$ **do**
30:   **if** $c \geq fr\_threshold$ **then**
31:     $bg\_points \leftarrow bg\_points \cup \{(x,y,z)\}$
32:   **end if**
33: **end for**
34: **return** bg_points

Each index of *r_map* contains a kd-tree where each leaf of the kd-tree takes a 4-tuple value (x,y,z,c), where (x,y,z) represents the 3-D coordinates of the projected point, and c is the frequency of that point across all frames. Then, the algorithm processes each

(x,y,z) point from every point cloud frame p in $\mathcal{P}$ and computes its index (r,c) in *r_map* using the spherical projection described in Eq. 1 and 2 (lines 3-7). In line 8, the algorithm finds the nearest neighbor of (x,y,z) by performing a query in the kd-tree at index (r,c) of *r_map*. If a nearest neighbor is found within the given distance threshold D_t, the algorithm updates the frequency of that nearest neighbor in the kd-tree (lines 9-10). Otherwise, the algorithm inserts a new 4-tuple value $(x,y,z,1)$ into the kd-tree (lines 11-13) to indicate that this (x,y,z) point has not been observed in any previous frames.

Next, the algorithm computes the frequency threshold and separates the background points based on that threshold (lines 16-34). To do so, an empty map fr is initialized (line 16), where the key represents the frequency of the (x,y,z) points across all frames, and the value indicates how many times that frequency occurs in the *r_map*. The algorithm then iterates through each tuple (x,y,z,c) from the *r_map* and increments the frequency count for c in the map fr (lines 17-19). Subsequently, the frequency threshold *fr_threshold* is computed by analyzing the key-value pairs of the map fr and identifying the point where the slope of the frequency curve of point frequencies becomes positive (lines 20-27). Finally, in lines 28-34, the algorithm marks the (x,y,z) points with a frequency greater than or equal to *fr_threshold* as background points, stores them in the set *bg_points*, and returns the set.

Once the background points are identified, filtering them from a point cloud frame p is a straightforward process. Algorithm 2 describes the filtering procedure. The algorithm takes a point cloud frame p, from which the background points need to be filtered, a set of (x,y,z) points *bg_points* identified as backgrounds points, LiDAR vertical resolution ϕ_l, LiDAR horizontal resolution θ_l, LiDAR vertical field of view V, LiDAR horizontal field of view H, and a nearest neighbor distance threshold D_t and outputs a set of non-background (x,y,z) points. The algorithm works as follows:

Initially, the background points are transformed into 2-D space using the same spherical projection method as described in Algorithm 1, and they are stored in the range map *r_map* (lines 1-8). Subsequently, for each point (x,y,z) in the point cloud frame p, the algorithm computes its spherical projection (r,c) and searches for the nearest neighbor in the kd-tree indexed at (r,c) in *r_map* (lines 9-14). If no nearest neighbor is found within the specified distance threshold D_t, the point (x,y,z) is classified as a non-background point (lines 15-17). Consequently, the algorithm adds it to the set *nonbg_points* (line 16).

Algorithm 2: Background Filtering Algorithm.

Require: a point cloud frame p, a set of (x,y,z) points *bg_points*, LiDAR vertical resolution ϕ_l, LiDAR horizontal resolution θ_l, LiDAR V-FoV V, LiDAR H-FoV H, nearest neighbor distance threshold D_t
Ensure: A set of (x,y,z) points, which are kept as non-background points.
1: $rows \leftarrow \frac{V}{\phi_l}, cols \leftarrow \frac{H}{\theta_l}$
2: $r\_map(1:rows, 1:cols) \leftarrow \emptyset$
3: **for** each point $(x,y,z) \in bg\_points$ **do**
4: $\quad d \leftarrow \sqrt{x^2+y^2+z^2}$
5: $\quad r \leftarrow \lfloor \arccos(\frac{z}{d})/\phi_l \rfloor$
6: $\quad c \leftarrow \lfloor \arctan(\frac{x}{y})/\theta_l \rfloor$
7: $\quad insert(r\_map(r,c),(x,y,z))$
8: **end for**
9: $nonbg\_points \leftarrow \emptyset$
10: **for** each point $(x,y,z) \in p$ **do**
11: $\quad d \leftarrow \sqrt{x^2+y^2+z^2}$
12: $\quad r \leftarrow \lfloor \arccos(\frac{z}{d})/\phi_l \rfloor$
13: $\quad c \leftarrow \lfloor \arctan(\frac{x}{y})/\theta_l \rfloor$
14: $\quad (x_n,y_n,z_n) \leftarrow NN(r\_map(r,c),(x,y,z),D_t)$
15: $\quad$ **if** $(x_n,y_n,z_n) = \emptyset$ **then**
16: $\quad\quad nonbg\_points \leftarrow nonbg\_points \cup \{(x,y,z)\}$
17: $\quad$ **end if**
18: **end for**
19: **return** *nonbg_points*

After processing all points in frame p, the algorithm returns the set *nonbg_points* as the output (line 19).

3.3 Network-Aware Compression

Background filtering achieves significant temporal compression (discussed in Section 4.5) by removing repeated background points across multiple frames. To further reduce the size of the data, we perform spatial compression on the filtered point cloud frames by using 3-D plane fitting method. Since most of the real-world surfaces are 3-D planes e.g., sides of cars, ground, etc., all points that lie on the same plane can be encoded by using that plane. We can also approximate non-plane surfaces by using a set of planes.

As discussed in (Feng et al., 2020), a plane in 3-D Cartesian space can be represented as:

$$x + ay + bz - c = 0, \tag{3}$$

where $(1,a,b)$ is the normal vector of the plane and $\frac{|c|}{\sqrt{1+a^2+b^2}}$ is the distance from the origin i.e., center of the LiDAR. Hence, we can encode all points on the same plane with just three coefficients. Since the exact position of each point on the plane is not explicitly encoded, we need to perform a ray casting process to find the intersection of a ray and the plane to reconstruct the position of a point.

To find the points that may lie on the same plane, we utilize the range map conversion of the point cloud. As adjacent grids in the range map correspond to consecutive scans from the LiDAR, the points mapped to them are likely to lie on the same plane. We initially partition the range map into uniform unit sub-grids, for example, 4×4 in size. The process begins with fitting a plane to the points within the first sub-grid and progressively extends to fit neighboring sub-grids, effectively creating a larger sub-grid. During each expansion step, we evaluate whether the current plane fitting can satisfactorily represent all the points within the newly enlarged sub-grid, adhering to a predefined threshold. If the criteria are met, all the points in the expanded sub-grid are encoded using the same plane coefficients. In cases where the criteria are not met, we restart the process from the current sub-grid and continue until all sub-grids within the range map have been processed.

Expressing the task of fitting a plane to a set of points can be naturally framed as a linear least squares problem (Nievergelt, 1994). Although traditional iterative approaches like RANSAC (Fischler and Bolles, 1981) are commonly employed, we use closed-form solution as suggested by (Feng et al., 2020) because it requires less computation and the computations can be parallelized.

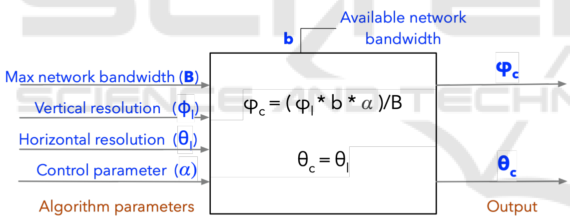

Figure 5: Network-aware module to adapt compression rate with available network bandwidth.

Finally, to make the compression network-aware, we vary the size of the range map according to the available network bandwidth while converting from the filtered point cloud frame. The idea is that a smaller range map would yield a higher compression rate and vice versa. Recall that, the dimensions of the range map depend on the vertical and horizontal resolutions of the LiDAR, denoted as ϕ_l and θ_l, respectively. We introduce two parameters ϕ_c and θ_c, initially set as ϕ_l and θ_l, respectively. Subsequently, we modify these parameters to change the dimensions of the range map, thereby enabling us to regulate the compression rate (see Figure 5). How to effectively tune these parameters in response to the available network bandwidth is detailed in Section 4.7.

4 EXPERIMENTAL EVALUATION

In this section, we provide a comprehensive empirical assessment of the proposed technique using several real-world datasets, comparing its performance with various baseline methods.

4.1 Evaluation Setup

We employ LiDAR sensors from three different vendors in our evaluation: Neuvition Titan M1, Livox Mid-70, and Ouster OS-1. This choice allows us to demonstrate the sensor-agnostic nature of our compression method. Neuvition and Ouster LiDARs exhibit repetitive scanning patterns, whereas the Livox LiDAR employs a non-repetitive scanning pattern. A summary of the sensor configurations that include the horizontal field of view (H-FoV), the vertical field of view (V-FoV), the frame rate and the scan pattern is described in Table 1.

Table 1: Sensor configurations.

Vendor	H-FoV	V-FoV	Frame rate	Scan pattern
Neuvition Titan M1	45°	25°	10 Hz	Repetitive
Livox Mid-70	70.4°	70.4°	10 Hz	Non-repetitive
Ouster OS-1	360°	45°	10 Hz	Repetitive

We connect the LiDAR to a Raspberry Pi with Ubuntu as the edge unit and run our compression system on it. The point cloud frames generated by the LiDAR sensor are processed using various libraries such as OpenCV, Boost, and PCL (Rusu and Cousins, 2011). To stream the compressed data to an edge server, we utilize a Celona private 5G wireless setup.

4.2 Evaluation Datasets

We have collected three real-world datasets (NEC-Neuvition, NEC-Livox, NEC-Ouster) from two different locations in New Jersey, USA. We mounted the Neuvition Titan M1 and Livox Mid-70 sensors together on a tripod and placed the tripod at the intersection of Independence Way and U.S. 1 Highway in Princeton, NJ. We recorded 10 minutes of data from both sensors at a frame rate of 10 Hz. Additionally, we recorded another 15 minutes of data at a 10 Hz frame rate using the Ouster OS-1 sensor. We placed the OS-1 sensor on a tripod at the intersection of Raymond Rd and Deerpark Dr in Monmouth Junction, NJ, and configured it with 64 vertical scans and 2048 horizontal scans.

Furthermore, we have used a publicly available dataset called StreetAware (Piadyk et al., 2023), which uses an Ouster OS-1 sensor configured with 16 vertical scans and 1024 horizontal scans to collect the data from various locations in Brooklyn, New York.

4.3 Baseline Methods

Since our system has two different components, we compare both of them to state-of-the-art works in their respective domains to demonstrate the necessity of these components.

4.3.1 Background Detection and Filtering

3D-DSF (Wu et al., 2018). This method divides the entire 3D space into small cubes and calculates the point density of each cube over a span of 20-30 minutes of frames. Subsequently, it determines a density threshold to distinguish between background points and moving object points.

RA (Lv et al., 2019). A raster-Based background filtering method for roadside LiDAR data, which performs four steps: region of interest (ROI) selection, rasterization into small cubes, background area detection, and background array generation.

DV (Zhao et al., 2023). A density variation-based background filtering algorithm for low-channel roadside LiDAR data. In this method, the detected area is initially segmented into small cubes, and their densities are computed. Next, an index is constructed to distinguish the area through which road users are passing. Outliers are then removed using the DBSCAN algorithm, and the LiDAR points that do not belong to the passing area are filtered.

4.3.2 Compression

G-PCC (Lasserre et al., 2019). A point cloud compression standard proposed by the MPEG, which is explicitly designed for compressing LiDAR point cloud data. This standard involves the creation of an Octree representation for point clouds and subsequent encoding of the Octree.

Draco (Google, 2018). This algorithm is developed by Google for compressing 3-D geometric meshes and point clouds. It uses various complex techniques such as edgebreaker (Rossignac et al., 2001), kd-tree, quantization, etc., to compress the point clouds.

Bf+(G-PCC/Draco). We also create two other baselines in which we filter the background points from the point cloud frame and then apply either G-PCC or Draco for compressing the background-filtered frame. The purpose of these baselines is to assess the effectiveness of our proposed background filtering method in conjunction with existing state-of-the-art compression algorithms.

4.4 Background Filtering Comparison

We compare our proposed background detection and filtering method with baseline algorithms in three dimensions: required memory, background point detection time, background point filtering time for each frame, and filtering accuracy. We use the NEC-Ouster dataset for this experiment because the Ouster OS-1 offers higher resolution and a wider field of view (FoV) compared to other sensors. Table 2 summarizes our findings for this experiment.

In Table 2, we observe that our method consumes only 20 MB of memory, which is about 40 times lower than the best baseline, 3D-DSF, requiring 820 MB of memory. This significant difference arises from the fact that the baseline methods divide the entire 3D space (LiDAR's detection range) into small cubes and employ a large 3D array to compute cube densities. In contrast, we convert the 3D points into 2D space and then calculate their frequencies. Consequently, our method requires significantly less memory compared to the baselines, making it suitable for deployment on low-cost devices.

In terms of background point detection time, Table 2 shows that our method performs almost as well as the best baseline. The background construction time depends on the number of frames the method observes to identify background points. Although our method takes slightly more time than the baseline, it is important to note that background detection is a one-time task, only need to rerun if the sensor's position changes. Therefore, the slightly increased time for background detection is negligible. A more critical factor is the time required to filter background points from each frame. From Table 2, our method outperforms the baseline methods, requiring only 5 ms per frame for background filtering. The baseline methods search within the set of background points to identify whether a point is part of the background or not. In contrast, our method converts the background points into a range map and then uses it to filter new frame points. As a result, our method achieves significantly lower filtering times. Since a LiDAR typically generates a frame every 100 ms, our method leaves ample time to apply our compression method and enables

Table 2: Background detection and filtering performance comparison.

Method	Memory	Detection time	Filtering time	Filtering accuracy
Ours	20 MB	120 s	5 ms	97%
3D-DSF	820 MB	1500 s	120 ms	96%
RA	1600 MB	1200 s	100 ms	97%
DV	850 MB	100 s	55 ms	97%

Table 3: Compression factor comparison of each method on various datasets.

	StreetAware	NEC-Livox	NEC-Neuvition	NEC-Ouster
Ours	45.40	35.36	80.78	66.61
Draco	17.35	15.56	26.11	20.54
G-PCC	9.67	7.53	13.29	11.82
BF-Draco	30.23	25.66	31.34	40.23
BF-GPCC	22.45	18.13	39.78	27.80

real-time streaming.

Finally, we demonstrate the effectiveness of our proposed method by assessing the accuracy of background filtering. To establish a ground truth dataset, we randomly select 50 frames from the dataset and manually annotate the vehicles and pedestrians in each frame, marking all other points as background. The filtering accuracy is presented in Table 2. It is evident that our method achieves a 97% accuracy rate, similar to the baseline methods.

4.5 Compression Quality

We compare our compression system with two state-of-the-arts point cloud compression algorithms: G-PCC (Lasserre et al., 2019) and Draco (Google, 2018). In addition, we create two other baselines: BF-GPCC and BF-Draco, where G-PCC and Draco are applied on top of our background filtering technique. The purpose of these two baselines is to show utility of our proposed filtering method. For quantitative comparison, we use compression factor as our evaluation metric, which is computed as the ratio of file sizes before and after compression. We run the methods on four real-world datasets: NEC-Ouster, NEC-Neuvition, NEC-Livox, and StreetAware.

Table 3 describes the compression rates obtained by each method for each dataset. We observe that our method consistently achieves the highest compression rates across all datasets, outperforming the baselines by compressing at least 2.5 times more effectively. For instance, our method attains a compression factor of 66.61 on the NEC-Ouster dataset, while Draco and G-PCC achieve 20.54 and 11.82, respectively.

From Table 3, we also note that applying Draco and G-PCC to the background-filtered data results in significantly higher compression factors than applying them to the raw data, respectively. To be more specific, BF-Draco achieves a 1.5 times higher compression than Draco, while BF-GPCC achieves a 2 times higher compression than G-PCC. This observation underscores the effectiveness of our background filtering technique.

Next, we evaluate the reconstruction errors of the decompressed frames produced by all methods. To do so, we use two metrics: Normalized Error (NE) and Structural Similarity Index Measure (SSIM) (Wang et al., 2004). The normalized error is computed as follows:

$$NE = \frac{1}{n}\sum_{i=1}^{n} \frac{NN(\mathcal{R}_i, \mathcal{D})}{\sqrt{(\mathcal{R}_{i,x})^2 + (\mathcal{R}_{i,y})^2 + (\mathcal{R}_{i,z})^2}}, \quad (4)$$

where, $\mathcal{R}$ is the raw point cloud frame, $\mathcal{D}$ is the decompressed frame, n is the total number of 3-D points in $\mathcal{R}$, and $NN(\mathcal{R}_i, \mathcal{D})$ is the nearest neighbor distance of i^{th} point in $\mathcal{R}$ among all points in $\mathcal{D}$.

While the normalized error measures the average deviation of the reconstructed points from the original points, the Structural Similarity Index (SSIM) assesses the similarity between two 2D images by evaluating the degradation of structural information. As point cloud frames inherently contain 3D information, we convert both the original and decompressed frames into 2D range images (Feng et al., 2020) and subsequently calculate the SSIM between them. The SSIM ranges from -1 to 1, where 1 indicates perfect similarity, 0 indicates no similarity, and -1 indicates perfect anti-correlation. Figure 6 shows the average normalized error and SSIM values of the decompressed frames for each method.

From Figure 6(a), it is evident that our method achieves the lowest normalized error while maintaining the highest compression ratio. The same trend holds true for the SSIM metric, as shown in Figure 6(b). Our method attains an SSIM value of 0.99, indicating that the structural integrity of the original frame is preserved nearly unchanged in the decompressed frame. In Figure 6, it is interesting to note that

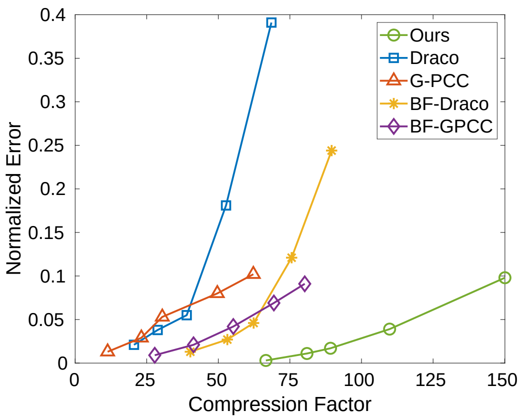

(a) Normalized error

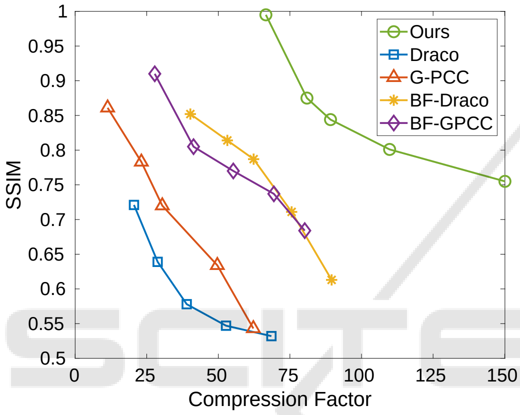

(b) SSIM

Figure 6: Reconstruction error of each method for different compression factors.

BF-Draco and BF-GPCC exhibit lower reconstruction errors than Draco and G-PCC, respectively. Since backgrounds are filtered in BF-Draco and G-PCC, the frames contain less noise, resulting in reduced reconstruction errors.

4.6 Communication Efficiency

The primary objectives of our proposed compression system include enabling real-time streaming and facilitating massive device connectivity across multiple traffic intersections through a shared private 5G network. To this extent, we examine two key aspects: the average compression time per frame for each method and the number of LiDARs that can be streamed using each method.

4.6.1 Compression Speed

Typically, a LiDAR sensor generates a frame every 100 milliseconds (ms). Therefore, the compression time must be less than 100 ms to enable real-time streaming without any frame drops. Figure 7 shows the compression time of each method. Our method takes only 20 ms to compress a frame, which is way below the latency requirement of streaming LiDAR data in real-time. Draco has similar compression speed to ours, however, it fails to match our compression rate.

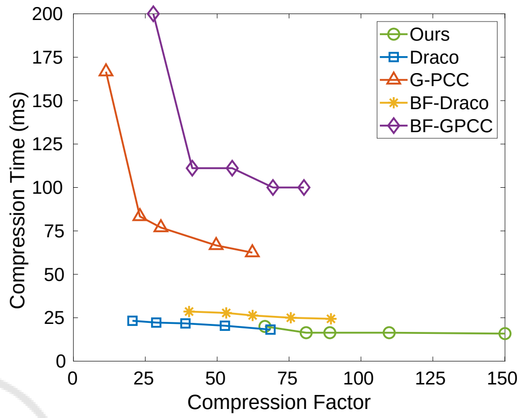

Figure 7: Compression speed comparison of each method for different compression factors.

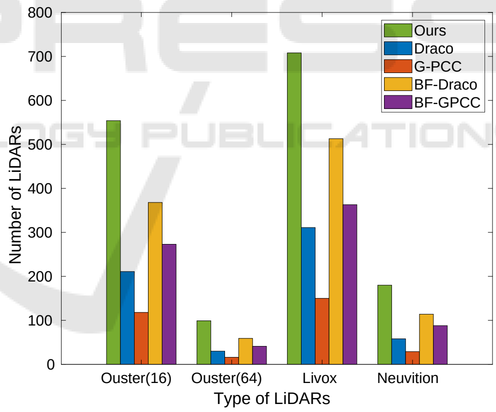

Figure 8: Number of supported LiDARs using each method considering 250 Mbps private 5G bandwidth.

4.6.2 Number of Streamed LiDARs

Considering the bandwidth of a shared private 5G network is 250 Mbps, Figure 8 illustrates how many LiDAR devices from different vendors can be streamed using each method. In Figure 8, we can observe that our method enables the transmission of data from hundreds of LiDAR sensors, regardless of vendor types, through a shared private 5G network. This represents at least 2.5 times more capacity than the baselines.

4.7 Parameter Sensitivity for Network Awareness

In this section, we will discuss how we can adjust the compression rate according to the available network bandwidth by compromising a tolerable level of compression quality. Our algorithm relies on two parameters, ϕ_c and θ_c, which control the dimensions of the range map. Increasing these parameters reduces the size of the range map, resulting in a higher compression rate but lower compression quality. To achieve the best compression quality, we set ϕ_c and θ_c to ϕ_l and θ_l, respectively, which correspond to LiDAR's vertical and horizontal resolutions. Consequently, when we have access to the full network bandwidth, these values remain unchanged. However, during network congestion, we have the flexibility to increase either ϕ_c or θ_c to boost the compression rate. Figure 9 shows the impact of increasing one of these parameters while keeping the other constant on the reconstruction errors, specifically, the normalized error.

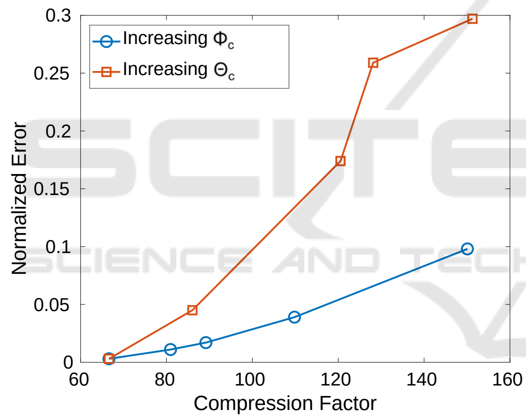

Figure 9: Parameter sensitivity test to identify which parameter is best to control compression rate with varying network bandwidth.

In Figure 9, the blue curve depicts the compression factor and the corresponding normalized error when θ_c is held constant while ϕ_c is set to ϕ_l, $1.25*\phi_l$, $1.5*\phi_l$, $1.75*\phi_l$, and $2*\phi_l$. For the orange curve, ϕ_c remains fixed while θ_c is set to θ_l, $1.25*\theta_l$, $1.5*\theta_l$, $1.75*\theta_l$, and $2*\theta_l$. It is evident from Figure 9 that increasing ϕ_c leads to a gradual increase in the normalized error as the compression factor rises. However, increasing θ_c results in a rapid escalation of the normalized error. Consequently, we propose adapting ϕ_c according to the available network bandwidth to control the compression factor effectively.

4.8 Application Accuracy

Superior compression capability is not useful if downstream applications are adversely affected by the use of decompressed data, signifying the loss of valuable information during the compression process. To demonstrate the effectiveness of the decompressed data, we select two applications: i) vehicle counting, and ii) object tracking, and conduct an analysis of the accuracy of these tasks.

4.8.1 Vehicle Counting

Vehicle counting is a straightforward yet valuable application, as it assists in assessing traffic congestion. We employ the vehicle counting algorithm implemented by (Mollah et al., 2022), which utilizes the DBSCAN clustering algorithm on the background-filtered data. To establish the ground truth dataset, we randomly select 100 point cloud frames and manually count the number of vehicles in each frame. Figure 10 illustrates the vehicle counting accuracy of each method at different compression factors.

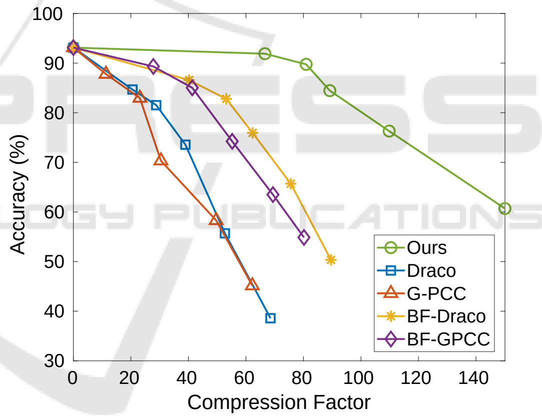

Figure 10: Vehicle counting accuracy using decompressed data produced by each methods.

In Figure 10, we observe that the application achieves an accuracy of 93% using raw data. In contrast, when using the decompressed data generated by our method, the application achieves a 92% accuracy at a 66x compression factor, indicating minimal loss of valuable information. In the case of G-PCC, the application accuracy is 88%, but the compression factor is only 11x. For Draco-decompressed data, the highest accuracy achieved is 85% with a compression factor of 20x. Across all methods, the accuracy of the application decreases as the compression rate increases. However, our method exhibits the lowest accuracy reduction rate compared to other baseline methods.

4.8.2 Object Tracking

For the object tracking application, we employ the PointNet deep learning model (Charles et al., 2017) to detect and track objects. Due to the absence of ground truth labels, we utilize the tracking results on the raw data as the ground truth. To assess the performance of each method, we use the Multiple Object Tracking Accuracy (MOTA) as the metric, which is computed as follows:

$$MOTA = 1 - \frac{\sum_t FN_t + FP_t + ME_t}{\sum_t GT_t}, \quad (5)$$

where, FN = false negatives, FP = false positives, ME = missmatch errors, and GT = ground truth object count. MOTA ranges from -inf to 1, where values close to 1 suggest good accuracy, while values close to 0 or less than 0 indicate poor accuracy.

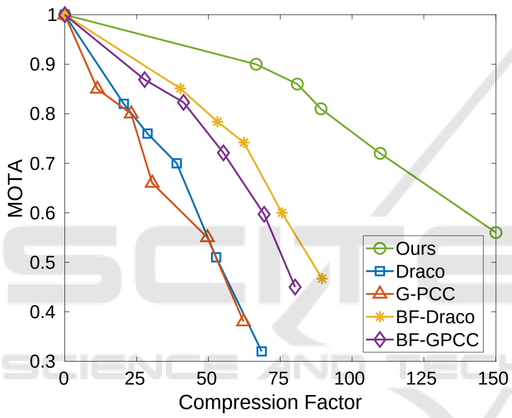

Figure 11: Object tracking accuracy using decompressed data generated by each method.

Figure 11 illustrates the object tracking performance of each method for various compression factors. Since the results of the raw data are considered as ground truth, the MOTA value is 1.0 for no compression. The decompressed data produced by our method achieve a MOTA value of 0.90, which is slightly lower than the tracking results of the raw data. However, it is still satisfactory, as the baseline methods obtain a MOTA value of up to 0.85 with significantly lower compression rates than ours.

5 CONCLUSION

In this paper, we propose a real-time compression method for roadside LiDAR data. Our method exploits the unique characteristic of roadside LiDAR data that the background points are repeated across all frames. We first detect and send the background points to the edge servers only once. Then, we filter the background points for each frame and only compress the filtered frames. This achieves substantial temporal compression and significant spatial compression. Our method is sensor-agnostic, fast, memory-efficient, and adaptive to varying network conditions. It achieves 2.5x higher compression rates and 40% better application-level accuracy than the state-of-the-art methods. Experimental results show that our method is effective in compressing roadside LiDAR data while maintaining high accuracy. It can be used to stream raw data from sensors across multiple intersections in real time, enabling a wide range of ITS applications.

REFERENCES

Charles, R., Su, H., Kaichun, M., and Guibas, L. J. (2017). Pointnet: Deep learning on point sets for 3d classification and segmentation. In *2017 IEEE Conference on Computer Vision and Pattern Recognition (CVPR)*, pages 77–85, Los Alamitos, CA, USA. IEEE Computer Society.

Feng, Y., Liu, S., and Zhu, Y. (2020). Real-time spatio-temporal lidar point cloud compression. *2020 IEEE/RSJ International Conference on Intelligent Robots and Systems (IROS)*, pages 10766–10773.

Fischler, M. A. and Bolles, R. C. (1981). Random sample consensus: A paradigm for model fitting with applications to image analysis and automated cartography. 24(6).

Golla, T. and Klein, R. (2015). Real-time point cloud compression. In *2015 IEEE/RSJ International Conference on Intelligent Robots and Systems (IROS)*, page 5087–5092. IEEE Press.

Google (2018). Draco: 3d data compression. https://google.github.io/draco/.

Guan, F., Xu, H., and Tian, Y. (2023). Evaluation of roadside lidar-based and vision-based multi-model all-traffic trajectory data. *Sensors*, 23(12).

Krivokuća, M., Chou, P. A., and Koroteev, M. (2020). A volumetric approach to point cloud compressionp̃art ii: Geometry compression. *Trans. Img. Proc.*, 29:2217–2229.

Lasserre, S., Flynn, D., and Qu, S. (2019). Using neighbouring nodes for the compression of octrees representing the geometry of point clouds. New York, NY, USA. Association for Computing Machinery.

Li, S. and Yoon, H.-S. (2023). Vehicle localization in 3d world coordinates using single camera at traffic intersection. *Sensors*, 23(7).

Lin, C., Zhang, H., Gong, B., Wu, D., and Wang, Y.-J. (2023). Density variation-based background filtering algorithm for low-channel roadside lidar data. *Optics & Laser Technology*, 158:108852.

Lv, B., Xu, H., Wu, J., Tian, Y., and Yuan, C. (2019).

Raster-based background filtering for roadside lidar data. *IEEE Access*, 7:76779–76788.

Mollah, M. P., Debnath, B., Sankaradas, M., Chakradhar, S., and Mueen, A. (2022). Efficient compression method for roadside lidar data. In *The 31st ACM International Conference on Information and Knowledge Management*, page 3371–3380.

Nievergelt, Y. (1994). Total least squares: State-of-the-art regression in numerical analysis. *SIAM Review*, 36(2):258–264.

Piadyk, Y., Rulff, J., Brewer, E., Hosseini, M., Ozbay, K., Sankaradas, M., Chakradhar, S., and Silva, C. (2023). Streetaware: A high-resolution synchronized multimodal urban scene dataset. *Sensors*, 23(7).

Rossignac, J., Safonova, A., and Szymczak, A. (2001). 3d compression made simple: Edgebreaker on a corner-table.

Rusu, R. B. and Cousins, S. (2011). 3D is here: Point Cloud Library (PCL). In *IEEE International Conference on Robotics and Automation (ICRA)*, Shanghai, China.

Sun, X., Ma, H., Sun, Y., and Liu, M. (2019). A novel point cloud compression algorithm based on clustering. *IEEE Robotics and Automation Letters*, 4(2):2132–2139.

Thanou, D., Chou, P. A., and Frossard, P. (2016). Graph-based compression of dynamic 3d point cloud sequences. *IEEE Transactions on Image Processing*, 25(4):1765–1778.

Tu, C., Takeuchi, E., Carballo, A., and Takeda, K. (2019). Point cloud compression for 3d lidar sensor using recurrent neural network with residual blocks. In *2019 International Conference on Robotics and Automation (ICRA)*, pages 3274–3280.

Wang, Z., Bovik, A., Sheikh, H., and Simoncelli, E. (2004). Image quality assessment: from error visibility to structural similarity. *IEEE Transactions on Image Processing*, 13(4):600–612.

Wu, J., Xu, H., Sun, Y., Zheng, J., and Yue, R. (2018). Automatic background filtering method for roadside lidar data. *Transportation Research Record*, 2672(45):106–114.

Zhao, J., Xu, H., Chen, Z., and Liu, H. (2023). A decoding-based method for fast background filtering of roadside lidar data. *Advanced Engineering Informatics*, 57:102043.

Zhao, J., Xu, H., Xia, X., and Liu, H. (2019). Azimuth-height background filtering method for roadside lidar data. In *2019 IEEE Intelligent Transportation Systems Conference (ITSC)*, pages 2421–2426.